Experimental Mechanics (2019) 59:349–359
https://doi.org/10.1007/s11340-018-00452-5

An Experimental Setup for Combined *In-Vacuo* Raman Spectroscopy and Cavity-Interferometry Measurements on TMDC Nano-resonators

S.S.P. Nathamgari [1,2] · S. Dong [1,2] · E. Hosseinian [1] · L.J. Lauhon [3] · H.D. Espinosa [1,2]

Received: 13 June 2018 / Accepted: 1 November 2018 / Published online: 21 November 2018

Abstract

Nanoelectromechanical (NEMS) systems fabricated using atomically thin materials have low mass and high stiffness and are thus ideal candidates for force and mass sensing applications. Transition metal dichalcogenides (TMDCs) offer certain unique properties in their few-layered form – such as piezoelectricity and a direct band gap (in some cases) – and are an interesting alternative to graphene based NEMS. Among the demonstrated methods for displacement transduction in NEMS, cavity-interferometry provides exquisite displacement sensitivity. Typically, interferometric measurements are complemented with Raman spectroscopy to characterize the number of layers in 2D materials, and the measurements necessitate high vacuum conditions to eliminate viscous damping. Here, we report an experimental setup that facilitates both Raman spectroscopy and interferometric measurements on few-layered Tungsten Disulfide (WS_2) resonators in high vacuum ($<10^{-5}$ Torr) conditions.

Keywords 2D materials · Nanoelectromechanical systems (NEMS) · Transition metal dichalcogenides (TMDCs) · Cavity-interferometry · Resonator

Introduction

Owing to their unique electromechanical, chemical and optical properties, two-dimensional (2D) materials have generated substantial research activity during the last decade. Starting with graphene in 2004, the field has been witnessing a steady rise in the variety of 2D materials as well as their applications. The absence of certain desirable properties in graphene – such as plasticity [1], piezoelectricity [2] or a tunable electronic bandgap [3] – has motivated the search for other, more exotic 2D materials [4, 5]. Group VI transition metal dichalcogenides (TMDCs), with the general formula MX_2 (where M = Mo, W and X = S, Se, Te), are one such category of materials that has received a lot of attention recently. Atomically thin TMDCs exhibit electromechanical properties that are strikingly different when contrasted with their bulk counterparts. Some TMDCs (for e.g. MoS_2) transition from an indirect to a direct band-gap semiconductor as the thickness is reduced to a monolayer [3]. This has allowed the realization of photodetectors with ultrahigh responsivity [6], excitonic lasers [7, 8] among other demonstrations. Additionally, the ability to tune the band-gap (up to 60 meV, [9, 10]) using mechanical strain opens up applications in photovoltaics [11]. Lastly, the absence of inversion symmetry in monolayer TMDCs leads to an in-plane piezoelectric coefficient that is comparable to commonly used bulk piezo-crystals like quartz and wurtzite [12, 13]. In addition to device applications, TMDCs have served as a platform for exploring several interesting phenomena including the valley Hall effect [14, 15], second harmonic generation [16, 17] and structural phase transitions induced by electrostatic doping [18].

By virtue of their high elastic stiffness and low mass, nanoelectromechanical systems (NEMS) fabricated using 2D materials – such as graphene [19], graphene oxide (GO) [20] and TMDCs [21, 22]– have fundamental resonance frequencies in 1-200 MHz range. Thus, they are promising candidates for force/mass sensing and RF-signal processing applications. When compared to

S. S. P. Nathamgari and S. Dong contributed equally to this work.

Electronic supplementary material The online version of this article (https://doi.org/10.1007/s11340-018-00452-5) contains supplementary material, which is available to authorized users.

✉ H.D. Espinosa
espinosa@northwestern.edu

[1] Department of Mechanical Engineering, Northwestern University, Evanston, IL 60208, USA

[2] Theoretical and Applied Mechanics Program, Northwestern University, Evanston, IL 60208, USA

[3] Department of Materials Science and Engineering, Northwestern University, Evanston, IL 60208, USA

micro-machined Si based and other one-dimensional (1D: nanowire, carbon nanotube) NEMS, resonators made of 2D materials provide unique advantages, such as a broad dynamic range [23, 24] and retained mechanical anisotropy as the thickness is reduced. For instance, the mechanical anisotropy in black phosphorus is one order of magnitude larger than that in Si. The anisotropy, as manifested in the resonant mode-shapes, can be utilized to resolve the crystal orientation in black phosphorus resonators [25, 26]. Lastly, 2D NEMS have served as avenues to explore an array of interesting non-linear phenomena such as phonon-cavity strong coupling [27–30], cavity side band cooling, parametric self-oscillations [31] and quintic non-linearity [32]. Within the domain of 2D resonators, TMDC based NEMS offer several advantages over graphene counterparts. First, the resonance frequency in monolayer TMDC resonators can be tuned using the piezoelectric effect instead of modulating the electrostatic back-gate voltage. Second, molecular dynamics (MD) calculations predict TMDC resonators to have better Q factors than graphene [33, 34]. Lastly, the dominant dissipation mechanism in undoped TMDC resonators is typically clamping losses that are independent of temperature and can be improved with optimized fabrication, rather than electrostatic interactions with the substrate, which is the case with graphene [35].

A common method of fabricating 2D resonators is to exfoliate a bulk-TMDC crystal using the scotch-tape method onto a Si substrate with pre-patterned holes or trenches. Because the exfoliation process results in flakes of different thicknesses, a prior characterization step is required before measuring the resonance spectra. Raman spectroscopy is a high-throughput, a non-contact method to characterize the layer number in some few-layered TMDC flakes and to distinguish monolayers in most TMDCs [36]. Additionally, resonant Raman spectroscopy has been used to investigate the electronic band-structure and phonon dispersion properties in TMDC crystals. Although several methods (optical, electrical, piezo/magneto-resistive) exist for NEMS actuation and motion transduction [37], cavity-interferometry has emerged as a popular, non-contact tool for detecting mechanical resonances in nano-resonators. Cavity-interferometry utilizes the underlying substrate as the reference mirror and the resonator as the moving mirror, obviating the need for an external reference arm such as that used in Michelson interferometry. Because the displacements involved are small (< 1 nm), the sample needs be in vacuum to eliminate any viscous damping effects. Here, we report a custom-built experimental set-up that can simultaneously perform both Raman spectroscopy and cavity-interferometry measurements on TMDC nano-resonators in high vacuum (< 50 μTorr). We fabricate resonators made of tungsten disulfide (WS_2) and characterize them using a combination of Raman spectroscopy and AFM. We use cavity-interferometry to measure both the driven resonance and the intrinsic thermal resonances due to Brownian motion at room temperature. Our results demonstrate that sub-micron thick TMDC resonators exhibit fundamental frequencies in the high frequency (HF, 3-30 MHz) and very high frequency (VHF, 30-300 MHz) spectrum and make high-responsivity (< 1 pm/Hz$^{0.5}$) cavity-interferometers, with potential applications in force/mass sensing and high frequency signal processing.

Experimental Methods

Fabrication of TMDC Nano-resonators

Microfabrication techniques were employed here to fabricate the target substrate with patterned cavities (called the device chip hereafter, see Fig. 1(b)) onto which exfoliated TMDC flakes were subsequently transferred. Figure 1 outlines the different steps in the fabrication protocol of TMDC resonators. A Si/SiO_2 (300 nm) wafer was spin-coated with a 100 nm thick positive e-beam resist (poly methyl methacrylate, PMMA C4, 1000 rpm for 45 s) and the interdigitated electrodes were patterned with an electron beam (Raith 150, 450 μC/cm^2 dose at 30 kV). The exposed PMMA was developed in a mixture of MIBK: IPA 1:3 for 30 s, followed by a gold deposition step (100 nm thick with 0.5 nm Cr and 5 nm Ti as adhesion layers) using e-beam evaporation. A standard lift-off process was then performed in anisole at 75 °C to remove PMMA so that only the desired Au electrode patterns were left on the Si/SiO_2 wafer (Fig. 1(b)). To further increase and control the cavity depth, reactive ion etching (Samco RIE 10NR) was used to selectively etch away approximately 200 nm of SiO_2 resulting in a final cavity depth of 300 nm. Few-layered TMDC flakes were mechanically exfoliated using the scotch-tape method that has been widely reported [38]. The exfoliated TMDC flakes were first transferred to a piece of gel-film that served as an intermediate carrier between the scotch tape and device chip to obtain better yield and less polymeric residue during the transfer process [39]. The gel-film was gently contacted with the device chip and moderate pressure was applied, then slowly detached from the device chip leaving the TMDC flakes adhered to the electrodes.

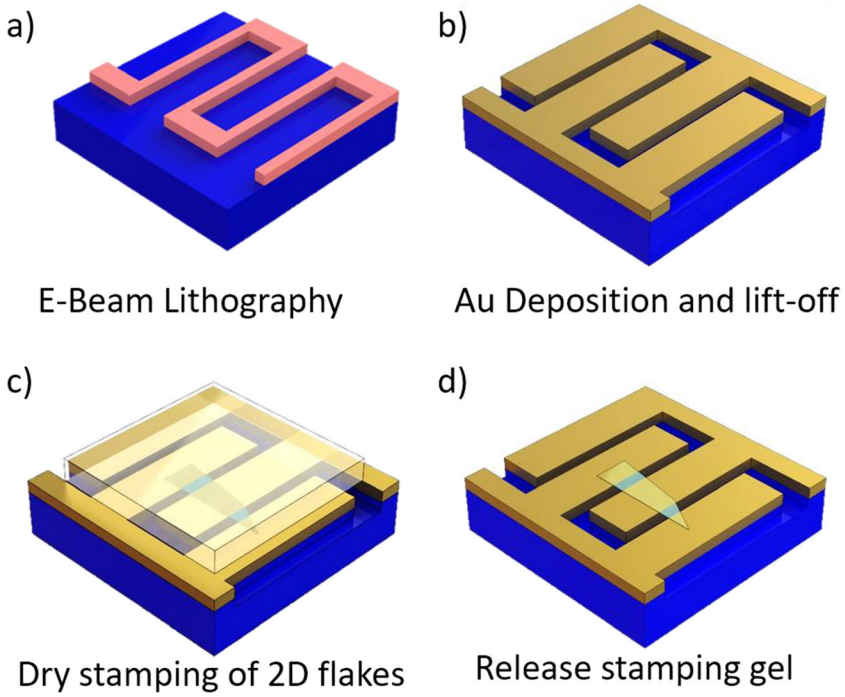

Fig. 1 Fabrication steps involved in making WS_2 resonators. (**a**) – (**b**). E-beam lithography, Au evaporation deposition, lift-off and reactive ion SiO_2 etch are performed sequentially to create the device chip. (**c**). Then, a dry stamping step is carried out where few-layered WS_2 flakes are attached to the bottom of the gel-film. (**d**). After the intermediate gel-film is removed, suspended WS_2 flakes are left on the electrodes due to van der Waal's adhesion with the gold surface

Characterization Techniques

Raman spectroscopy

Raman spectroscopic measurements were used in conjunction with other characterization methods (AFM, see below) to identify the number of layers in the exfoliated samples. A He-Ne red-laser (632.8 nm wavelength, avg. power < 450 μW) was focused to a spot size of less than 1.5 μm using a 50X long working distance (LWD) objective (N.A. 0.55). The reflected and scattered light were collected by the same objective and passed through a Rayleigh filter (efficient to <100 cm^{-1}) followed by a motorized Czerny-Turner spectrograph (1800 grooves/mm) that was coupled to a Peltier cooled EMCCD (Andor Newton). The spectral resolution of the system is <1 cm^{-1} and the peak centroids were identified by fitting the spectra to a multi-peak Lorentzian line shape.

Thickness measurement using atomic force microscopy (AFM)

An AFM cantilever probe (42 N/m stiffness and 320 kHz fundamental resonance frequency) was used in tapping mode on a Park XE-120 system to generate a topographical map of the TMDC flake. Line scans from multiple areas of the flake were averaged and the mean value is reported as the thickness.

Scanning electron microscopy (SEM)

Successful fabrication of device chips and the subsequent transfer of TMDC flakes was verified using a FEI Nova 600 SEM that was operated at 10 kV acceleration voltage.

In Vacuo Cavity-Interferometry Setup

Figure 2 shows the different components in our experimental setup which are described next. A custom designed chamber was used to achieve vacuum level of <50 μTorr in ~ 2 h using a turbo-molecular pump (HiCube 80 Eco). The vacuum level was measured using a pirani/cold-cathode gauge (Pfeiffer MPT 200). The sample was mounted on a vacuum compatible, XYZ piezo-actuator stack (Attocube ECS 3030) with nanometer spatial resolution. A multi-pin electrical feedthrough on the vacuum chamber allowed the application of the driving voltage to the PZT disk underneath the sample. The probe laser (He-Ne, 632.8 nm wavelength) was focused onto the sample to a spot size of less than 1.5 μm using a 50X long working distance (LWD) objective (N.A. 0.55). An anti-reflection coated viewport was used to minimize back-reflections and ghosting. The laser power was measured outside the vacuum chamber and was kept to <450 μW to minimize sample heating. The nano-resonator and the Si

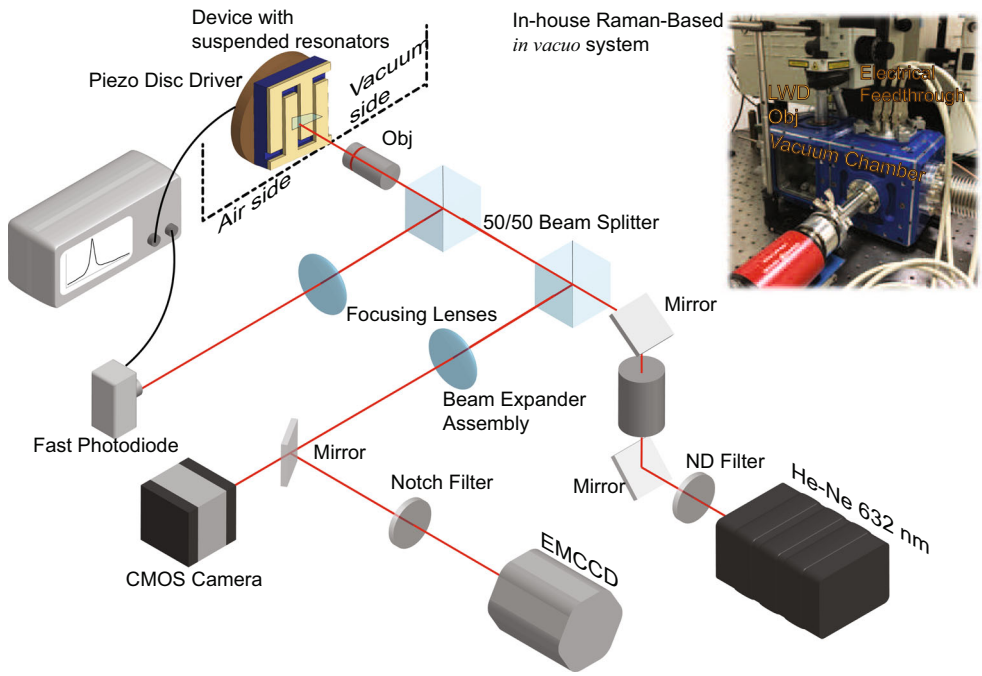

Fig. 2 Schematic showing the *in vacuo* optical setup for Raman spectroscopy and cavity-interferometry. The device chip is attached to a piezo-disc and mounted inside the vacuum chamber. Electrical and optical signals are coupled into and out of the chamber through electrical feedthroughs and an anti-reflective view-port, respectively. Free-space optical components are configured to enable simultaneous interferometry, Raman spectroscopy and optical microscopy

substrate underneath form an optical cavity whose reflectance was modulated by the motion of the resonator and is measured on a fast photodiode. An RF function generator (Agilent 33250a) was used to drive the PZT disk; the photocurrent generated on the photodiode was first amplified using a trans-impedance amplifier and then fed to the RF-input of a lock-in amplifier (SR844). A custom-written Python routine was used to communicate with the lock-in amplifier and the function generator using the GPIB and RS-232 serial interface, respectively. A spectrum analyzer (Rigol 815-TG) was used to measure the undriven thermomechanical resonances.

Results

Fabrication of WS_2 Resonators

The gold electrodes and etched SiO_2 offer good contrast in the SEM (Fig. 3) allowing the fabrication quality of the device chips to be easily inspected. 5 μm wide strips (pseudo colored yellow) in the images correspond to the gold electrodes whereas the narrower strips (2 μm wide) correspond to the trenches. To ascertain that the transferred TMDC flakes were not collapsed, the samples were tilted, and their projected side-views were observed. In addition, tapping mode AFM scans of the transferred flakes over the suspended region were performed (see SI, Fig. S2). The data indicate a maximum vertical deflection of ~ 18 nm, which is much smaller that the cavity depth of 300 nm. This confirms that the flakes were not collapsed, which is further corroborated by the resonator measurements.

The cavity depth is a crucial factor in determining the responsivity of the interferometer, where the responsivity (R) is defined as the change in reflectance per unit motion of the resonator, i.e. $= \frac{dI_r}{dz}$, where I_r is the intensity of the reflected light. A cavity depth of 300 nm was chosen to optimize the responsivity of the interferometer for a range of resonator thicknesses. A thin film interference model can be used to determine the cavity's responsivity (see Fig. 4). For a given intensity of incident light I_0, the intensity of the reflected light I_r from the optical cavity can be estimated using the following equation [40].

$$\frac{I_r}{I_0} = \left| \frac{r_1 e^{i(\phi_1+\phi_2)} + r_2 e^{-i(\phi_1-\phi_2)} + r_3 e^{-i(\phi_1+\phi_2)} + r_1 r_2 r_3 e^{-i(\phi_1-\phi_2)}}{e^{i(\phi_1+\phi_2)} + r_1 r_2 e^{-i(\phi_1-\phi_2)} + r_1 r_3 e^{-i(\phi_1+\phi_2)} + r_2 r_3 e^{-i(\phi_1-\phi_2)}} \right|^2$$

where r_1, r_2 and r_3 are reflection coefficients at the vacuum-resonator, resonator-vacuum and vacuum-substrate interface; and are given by the following relations (n_v, n_r, n_{Si} are the refractive index of vacuum, resonator and Si respectively).

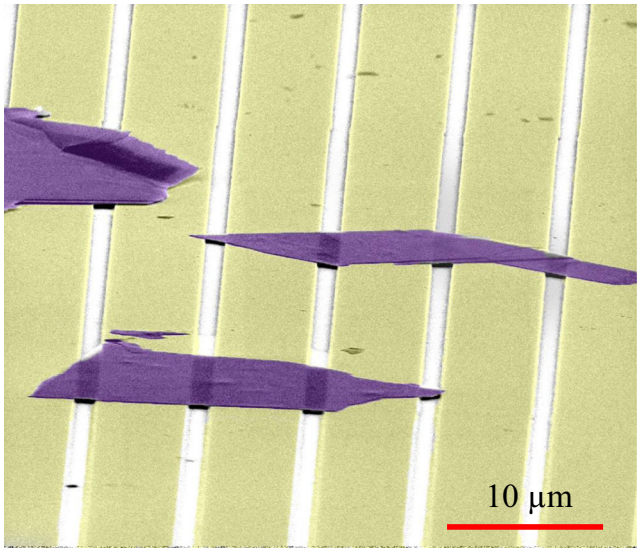

Fig. 3 A scanning electron micrograph of WS_2 resonators that were transferred to the device chip using mechanical exfoliation and dry transfer methods

$$r_1 = \frac{n_v - n_r}{n_v + n_r} \qquad r_2 = \frac{n_r - n_v}{n_r + n_v} \qquad r_3 = \frac{n_v - n_{Si}}{n_v + n_{Si}}$$

whereas ϕ_1 and ϕ_2 are the phase shift due to the resonator thickness and cavity depth, given by

$$\phi_1 = \frac{2\pi n_r d_r}{\lambda} \quad \phi_2 = \frac{2\pi n_v d_v}{\lambda}$$

In the phase-shift relations, d_r and d_v are the resonator thickness and the cavity depth, respectively, while λ is the wavelength of the probe laser (632.8 nm). In Fig. 4, the reflectance of the optical cavity was calculated for a monolayer (black, solid line), 10 layer (red line with circular marker) and 30 layer WS_2 resonator (blue, dashed line), using $n_{Si} = 3.881 - 0.0019i$, $n_r = 5.6104 - 0.7293i$ [41] and n_v=1. The slope of the curve at $d_v = 300$ nm determines the responsivity of the cavity. Several conclusions can be drawn from this analysis: the chosen cavity depth yields good responsivity values for resonator thicknesses ranging from a monolayer to 30 layers; the responsivity increases with increasing thickness; and finally, for some cavity depth values (the minima in the curves, near 360 nm), the responsivity can be close to zero and should be avoided.

Raman Spectroscopy and AFM Characterization

Here, we highlight the main features in the Raman spectrum of WS_2 that are utilized to infer the number of layers and point the reader to refs. [36, 42, 43] for a more in-depth discussion of the different phonon modes in TMDCs. The Raman spectrum of WS_2 is characterized by two first order modes at the Brillouin zone center, i.e. an in-plane E^1_{2g} mode and an out of plane of A_{1g} mode. In the E^1_{2g} mode, the tungsten (W) atom and the pair of sulfur (S) atoms vibrate away from each other; whereas in the A_{1g} mode, the S atoms move out of plane relative to W (see Figs. 5(b) and 6(b)). As the thickness of WS_2 is reduced, changes in interlayer interactions produce a well characterized softening (red-shift) of the A_{1g} mode and smaller (~1 cm^{-1}) non-monotonic shifts in the E^1_{2g} mode. Thus, the spacing between the two phonon modes serves as a useful metric for identifying the layer number, and a difference of 66 cm^{-1} between the two modes is indicative of a monolayer [42]. We note that the absolute positions of each of these modes depend differently on the presence of strain, dopants or impurities [44] induced during the fabrication step. As such, a one-time calibration of the spacing between the phonon modes as a function of the flake's thickness using AFM is necessary. Also, Raman spectroscopy is most useful in discerning the thickness of few-layered flakes (<10) and the frequency spacing quickly saturates for flakes that are much thicker than 10 layers.

The resonator flakes are imaged with an AFM in tapping mode using scan areas that are large enough

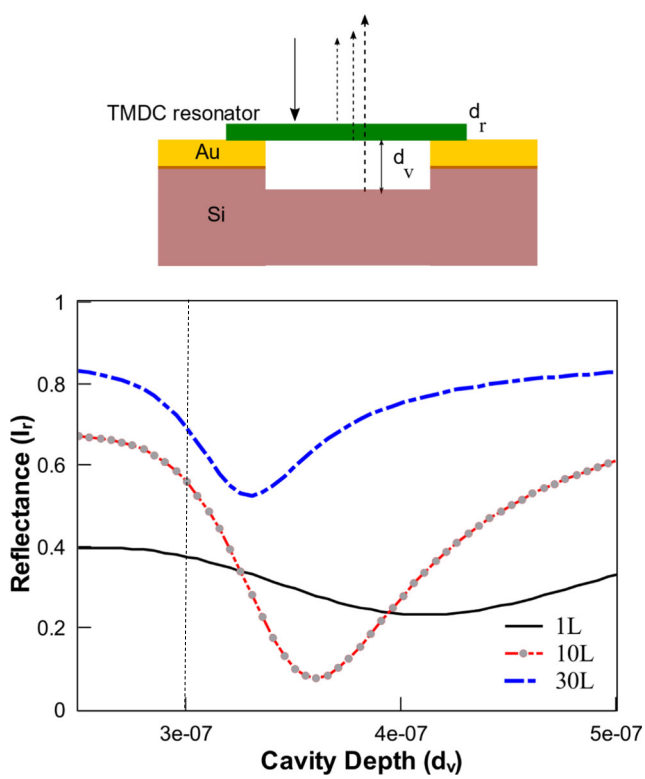

Fig. 4 Schematic showing the thin film interference model used to calculate the responsivity of the interferometer. Solid arrows indicate incident light and dashed arrows indicate the reflected light. A cavity depth (d_v) of 300 nm (dashed, vertical line in the bottom image) is chosen to maximize the responsivity. d_r denotes the resonator thickness

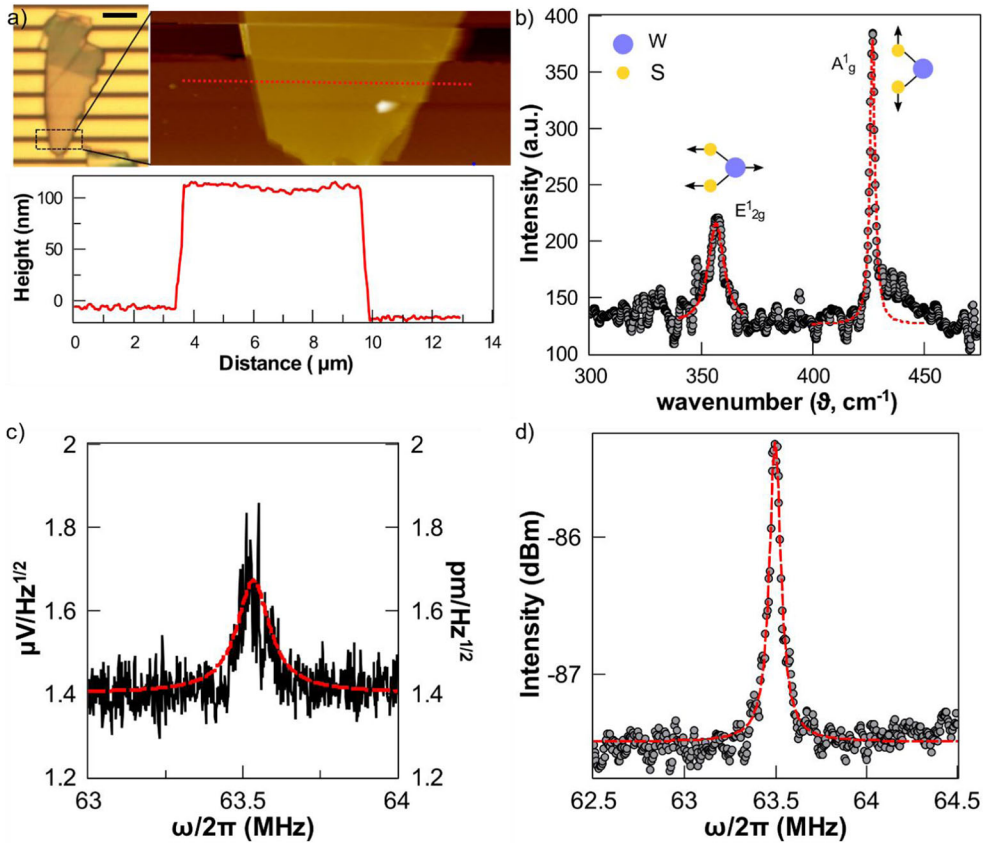

Fig. 5 (**a**) Optical micrograph (left, scale bar: 20 μm) and tapping mode AFM scan (right) to determine the thickness of the resonator (dashed box). The resonator is approximately 125 nm thick. (**b**) Raman spectrum showing the in-plane E^1_{2g} and out of plane A^1_g modes with a separation of >70 cm^{-1} indicating >10 layers. Red, dashed lines are a Lorentzian fit to the measured data, denoted by grey circles. (**c**) Thermomechanical resonance spectrum of the resonator with a fundamental frequency of 63.524 MHz and a Q-factor of 749. Black line indicates the measured displacement and the red, dashed line is a Lorentzian fit. (**d**) Driven oscillations of the resonator with a driving amplitude of 224 mV to the PZT disc; the dashed line is a Lorentzian fit to the raw data (grey circles)

to cover both the suspended region as well as that in contact with the electrodes. The uniformity in surface topography across the entire scan region indicates that the flake thickness is consistent across the suspended and adhered areas; so, the height measurements taken on the supported regions are used to characterize the thickness of the resonator. The three resonators reported in this manuscript have thickness values of 125 nm

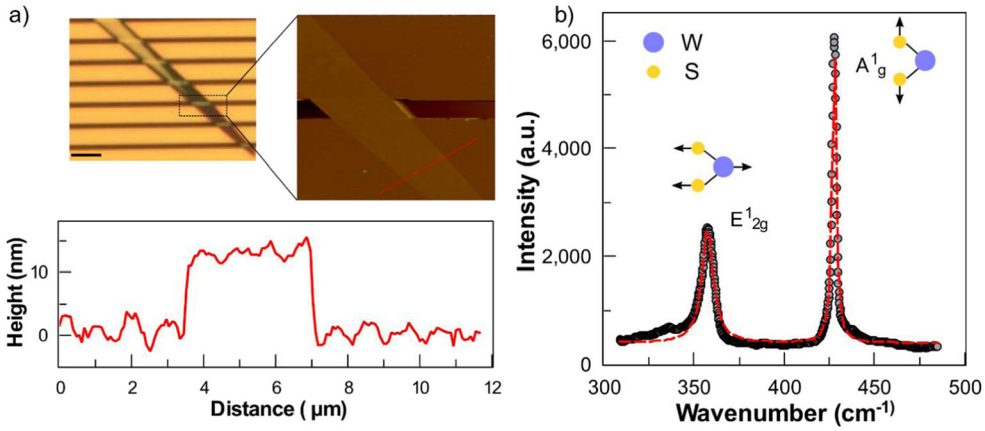

Fig. 6 (**a**) Optical micrograph (left, scale bar: 20 μm) and tapping mode AFM topography image (right) to determine the thickness of the resonator (dashed box). The resonator is approximately 12 nm thick. (**b**) Raman spectroscopy showing the in-plane E_{2g}^1 and out of plane A_g^1 modes with a separation ~ 70.24 ± 0.07 cm^{-1}. (Red, dashed lines indicate a Lorentzian fit to the measured data)

(Fig. 5(a)), 12 nm (Fig. 6(a)) and 7 nm (see SI, Fig. S1) respectively, as confirmed through AFM. Their corresponding frequency separation values between the phonon modes (A_{1g}, E^1_{2g}) are 72.5 cm^{-1}, 70.2 cm^{-1} and 69.8 cm^{-1}.

Cavity-Interferometry Measurements

We first discuss the measurement of thermomechanical resonances in WS_2 resonators. The thermal fluctuations in the position of the resonator modulate the depth of the optical cavity, and consequently the intensity of light reflected from the cavity. The light collection efficiency in our experimental setup is high enough to resolve the Brownian motion in the resonators without the need for external actuation. Figure 5(a) shows an optical micrograph of a WS_2 resonator that is 125 nm thick (186 layers), as confirmed by AFM topography scan (Fig. 5(a)) and Raman spectroscopy (Fig. 5(b)). Figure 5(c) presents the thermomechanical resonance spectrum of the fundamental mode of the resonator. By fitting the resonance data to a Lorentzian line-shape, we obtain $\omega_0/2\Pi = 63.524 \pm 0.002$ MHz and a Q-factor ~ 749. For a spring-dashpot system with a quality factor Q, effective mass M_e and resonance frequency ω_0, the displacement power spectral density (PSD) of the system, as a function of the frequency (ω), is given by

$$S_x^{0.5}(\omega) = \sqrt{\frac{4k_bT\omega_0}{QM_e}\frac{1}{\left(\omega_0^2-\omega^2\right)^2+\left(\omega_0\omega/Q\right)^2}}$$

where k_b is the Boltzmann constant and T is the temperature (K). On resonance, the displacement PSD reduces to $S_x^{0.5}(\omega_0) = \sqrt{\frac{4k_bTQ}{M_e\omega_0^3}}$. Assuming $T = 300$ K and using $M_e = 0.8\ M$, where M is the mass of the resonator (~ 16.88 pg), $S_x^{0.5}$ ~ 0.014 pm/$Hz^{0.5}$. The displacement PSD is transduced to a voltage PSD by the photodiode and backend electronics in the setup, and is given by

$$S_V^{0.5}(\omega) = \sqrt{\Phi^2\left[\frac{4k_bT\omega_0}{QM_e}\frac{1}{\left(\omega_0^2-\omega^2\right)^2+\left(\omega_0\omega/Q\right)^2}\right]+S_N}$$

Here, Φ (units of μV/pm) and S_N are the responsivity and noise floor of the photodiode-amplifier combination, respectively. The noise floor of our detection system is S_N ~ 1.4 μV/$Hz^{0.5}$, which when converted to displacement units yields a displacement sensitivity of 12 fm/$Hz^{0.5}$ and a responsivity of Φ ~ 117 μV/pm for the WS_2 resonator in Fig. 5. The displacement resolution in our setup is limited by the noise in the transimpedance amplifier. Figure 5(d) shows the driven response of the resonator using a drive voltage of 0 dBm (V_{rms} ~ 0.224 V) to the PZT disk; the dashed line is Lorentzian curve fit to the obtained data.

The resonance frequency of a thin-plate under tension can be expressed as $f = \sqrt{f_{membrane}^2 + f_{plate}^2}$. Here, the term $f_{membrane}$ is the contribution to the resonance frequency from a membrane model assuming negligible bending stiffness D ($D = \frac{E_Y h^3}{12(1-\nu^2)}$, where E_Y is the elastic modulus, h is the resonator thickness and υ is the Poisson's ratio), while f_{plate} is the contribution obtained from the elasticity solution by neglecting any prestress. Depending on the relative contributions from the two terms, the resonator could be in (1) the plate regime, where the bending rigidity dominates; (2) the membrane regime, where the behavior is governed predominantly by the prestress; or (3) a mixed-mode where both contributions are comparable and need to be accounted for. The expressions for $f_{membrane}$ and f_{plate} depend on the resonator geometry and the boundary conditions. For a resonator with a rectangular geometry, the general expression for f_{plate} is given by

$$f_{plate}^2 = \frac{\pi^2 D}{4a^4\rho}\left[G_x^4 + G_y^4\left(\frac{a}{b}\right)^2 + 2\left(\frac{a}{b}\right)^2\left\{\nu H_x H_y + (1-\nu)J_x J_y\right\}\right],$$

where the factors G_i, H_i and J_i ($i = x, y$) depend on the boundary conditions: a, b are the length and width of the resonator, respectively; ρ is the areal mass density; and ν is the Poisson's ratio. The expression has been derived using the Rayleigh-Ritz method in ref. [45]. For free-boundaries along the y direction and the fundamental mode, $G_y = H_y = J_y = 0$, and the equation simplifies to $f_{plate}^2 = \frac{\pi^2 D}{4a^4\rho}G_x^4$. $G_x = 1.0$ for the fundamental mode and simply supported edges along the x direction. $f_{membrane} = \frac{n}{2L}\sqrt{\frac{T}{2L}}$ for a 1-D string under tension, where n is mode number and T is the prestress. For the resonator shown in Fig. 5, assuming an isotropic elastic modulus of $E_Y = 270$ GPa (which is valid for strains less than 10%, [46]), $\nu = 0.25$ and $\rho = 7500\ h$ kg m^{-2}, f_{plate} ~ 70.24 MHz, which is close to the observed resonance frequency of 63.52 MHz and indicates that the resonator is in the plate regime.

Figure 6(a) shows an optical micrograph and AFM topography data of a WS_2 resonator that is 12 nm thick. Raman spectroscopy on the same resonator (Fig. 6(b)) yields a spacing of 70.24 ± 0.07 cm^{-1} between the in-plane E^1_{2g} mode and the out of plane of A_{1g} mode. Figure 7(a) shows the resonance spectra of the sample actuated with a driving voltage of +30 dBm (V_{rms} ~ 7 V) applied to the PZT disc. The first five modes of resonance have been indicated in Fig. 7(a) using vertical dotted lines. The displacement of the PZT disc is non-uniform and particularly pronounced in the 1-5 MHz span, which results in the large, non-uniform background for

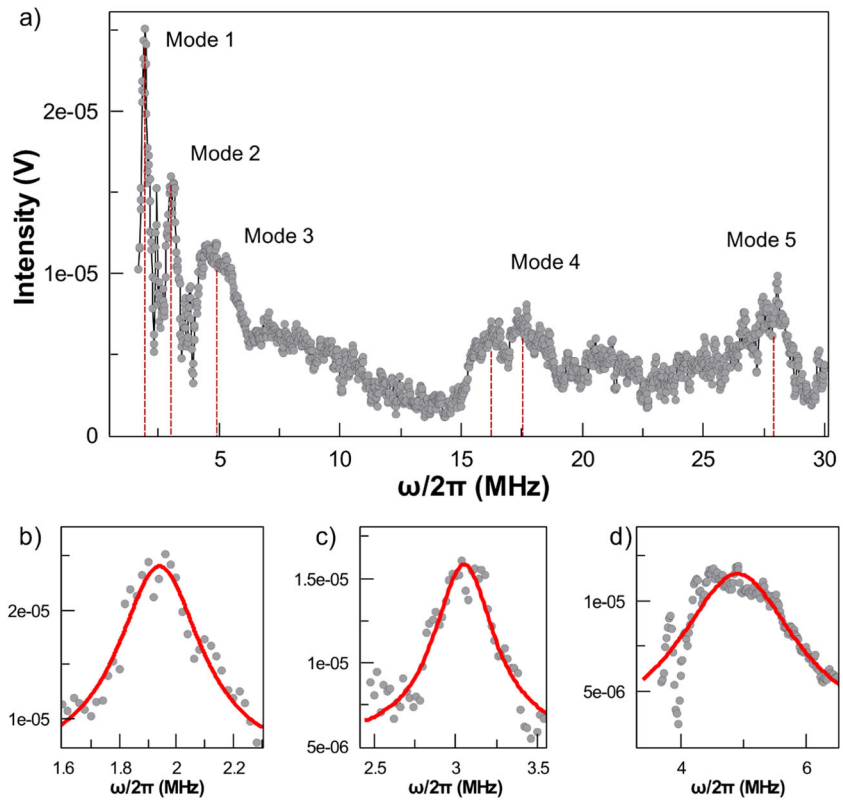

Fig. 7 (**a**) Voltage vs frequency plot showing the first five resonance modes of the 12 nm thick WS_2 resonator. A drive voltage of +30 dBm was applied to the PZT disc. A Lorentzian line-shape (red, solid line) was fit to the measured data corresponding to modes 1, 2 and 3 in (**b**), (**c**) and (**d**) respectively. The center frequency and FWHM of each mode are listed in Table 1

Modes 1-3 [47]. The two closely spaced resonance modes near 17 MHz are both attributed to Mode 4. Figures 7(b-d) show the measured data (grey circles) for the first three modes and a Lorentzian line-shape fit (red, solid line) to each. Table 1 summarizes the peak-locations and the full width at half-maximum (FWHM) values for the first five modes. The smaller fundamental frequency, as compared to the 125 nm thick resonator, is consistent with the smaller bending rigidity as the thickness is reduced to 12 nm.

Figure 8 presents experimental data on a few-layered WS_2 resonator. AFM topography scan reveals the resonator thickness to be 7 nm (see SI Fig. S1), i.e. a total of 9 layers. Fitting the Raman spectroscopy data in Fig. 8(a) to a Lorentzian line-shape for each of the in-plane (E^1_{2g}) and the out of plane (A_{1g}) modes yields a spacing of 69.8 cm^{-1} between them, which can serve as calibration for identifying resonators with similar thickness. Figure 8(b) presents the fundamental mode of the WS_2 resonator with a peak centroid $\omega_0/2\Pi = 9.1 \pm 0.1$ MHz and full width at half maximum $\Delta\omega_0/2\Pi = 0.36$ MHz. The contribution from the bending stiffness to the fundamental mode's frequency can be estimated as $f^2_{plate} = \frac{\pi^2 D}{4a^4\rho}$, which yields $f_{plate} \sim 3.93$ MHz. The estimated value accounts for only ~ 20% of the observed value. This suggests that the resonator is in the mixed regime where contributions from both the prestress and bending stiffness are important. Using $f_{membrane} = \frac{1}{2L}\sqrt{\frac{T}{2L}}$, the average pre-stress in the resonator can be estimated as $T \sim 56.5$ mN/m, which is typical in suspended 2D materials (refs. [12, 22, 48]).

However, we also note that the actual geometry of the resonators is closer to a trapezoid than a rectangle. For trapezoidal and parallelogram plates, closed form solutions exist only for the case of simply supported boundaries. Here, we use the closed form solution for rectangular plates to arrive at an order of magnitude estimate for the fundamental mode. Indeed, resonators fabricated using 2D materials have previously shown to exhibit certain "transverse/edge modes" that

Table 1 Resonance frequencies and FWHM values for the first five modes of the 12 nm thick WS_2 resonator

Mode #	ω/2Π (MHz)	Δω/2Π (MHz)
1	1.94 ± 0.02	0.3 ± 0.1
2	3.03 ± 0.04	0.3 ± 0.1
3	4.94 ± 0.01	2.2 ± 0.8
4	16.28 ± 0.08	0.9 ± 0.4
	18.02 ± 0.07	2.5 ± 0.8
5	27.23 ± 0.02	3.1 ± 0.4

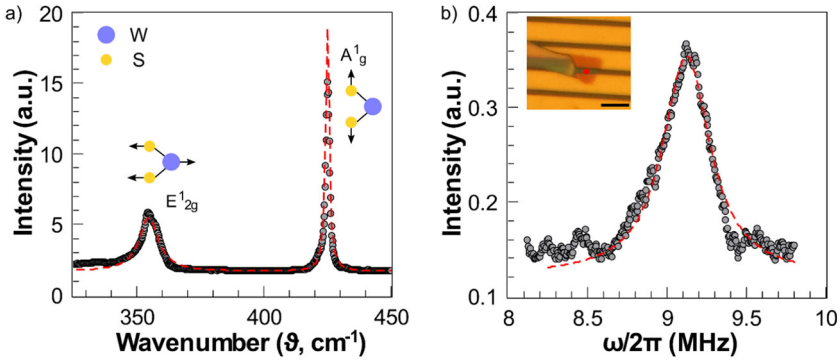

Fig. 8 (**a**) Raman spectroscopy characterization of a few-layered WS_2 resonator. The spacing between the in-plane E_{2g}^1 and out of plane A_g^1 modes is 69.8 cm^{-1}. AFM characterization reveals the thickness to be 7 nm (~ 9 layers, see SI). (**b**) The fundamental resonance mode under driven oscillations (~ 2 V_{rms} to the PZT disc) is shown where the red, dashed line is a Lorentzian fit to the measured data (grey circles). Inset shows an optical micrograph with scale bar = 10 μm, the red dot indicates the region on the resonator where the measurements were taken

can arise due to non-uniform strain induced during the fabrication procedure [49] and as such, the resonance frequencies cannot be accurately estimated without a priori knowledge of the mode-shapes. The addition of mode mapping would be a desirable feature to our experimental setup and will be the focus of future work.

Conclusion

In this report, we described a custom-built *in-vacuo* experimental setup for making combined Raman spectroscopy and cavity-interferometry measurements on TMDC resonators that were fabricated using mechanical exfoliation and dry transfer onto microfabricated device chips. As a proof of concept, we investigated the mechanical resonances in multi-layered WS_2 resonators shown to be in the plate-regime and a few-layered WS_2 resonator that was in the mixed-regime. One of the advantages of combining the two experimental techniques is the prevention of sample degradation, which can be particularly problematic for the selenides ($MoSe_2$, WSe_2) and tellurides ($MoTe_2$, WTe_2) in TMDC family. The combination allows us to not only encapsulate the exfoliated samples in an inert, high-vacuum environment but also to *identify* few-layered flakes (using Raman spectroscopy) in a high throughput manner for subsequent resonator measurements. Because of the sensitivity and the abundant data available on Raman characterization of 1-5 layered TMDC flakes (see Table 2 below), the reported experimental setup is best utilized when dealing with monolayers or few-layers, although their controlled, large-scale fabrication is presently a challenge. Raman spectroscopy can also serve as a *non-destructive, local* probe of motion and stress in nano-mechanical systems [50]. The softening of the in-plane phonon mode at different driving frequencies can be used as an indicator of both the resonance frequency as well as the local strain, although the bandwidth of our EMCCD detector (1 MHz) precludes us from implementing this functionality in our setup [50]. The device chips serve as a versatile platform for the investigation of resonators fabricated using other 2D materials and for implementing other actuation and detection modalities. For instance, although we have utilized piezo-actuation for driving the resonators in this study (primarily for its simplicity), the inter-digitated electrodes on the device chips can be exploited to implement capacitative actuation and all-electrical methods of detection, such as mixed-down and frequency modulation (FM) techniques. Lastly, the optical cavity formed by the resonator and underlying substrate can be

Table 2 Summary of important features in the Raman spectra of different few-layered TMDCs that can be utilized to infer the layer number. nL denotes a TMDC flake with "n" layers

TMDC	Features in Raman Spectra utilized to distinguish few-layered to monolayer flakes
MoS_2	The spacing between the E^1_{2g} and A_{1g} modes is 18, 22.4, 23.3 and 24.3 cm^{-1} for 1 L, 2 L, 3 L and 4 L respectively (ref. [36])
WS2	The spacing between the E^1_{2g} and A_{1g} modes is 65.5, 68.3 and 69.2 cm^{-1} for 1 L, 2 L and 3 L respectively (ref. [51])
MoSe2	The A_{1g} mode softens with decreasing thickness; starting from 242.5 cm^{-1} for 5 L, the mode redshifts to ~ 240.5 cm^{-1} for 1 L (ref. [52]). For 3 L to 5 L, the mode splits into two peaks, which can serve as an additional confirmation of the layer number
WSe2	The E^1_{2g} and A_{1g} modes coincide for 1 L; the separation increases from 1.5 cm^{-1} for 2 L to 3 cm^{-1} for bulk. Alternatively, the intensity ratio of A_{1g} and E^1_{2g} modes can be used to infer the number of layers (refs.[52, 53]), where the ratio increases with increasing thickness (~ 2.5 for 2 L and ~ 8 for bulk)
MoTe2	The B^1_{2g} mode, which is inactive in bulk form, is active in few-layered flakes but not in 1 L $MoTe_2$ (refs. [54, 55]). The intensity ratio of B^1_{2g} and E^1_{2g} modes can be used to distinguish 2 L-5 L flakes (ref. [54]). For 1 L, the absence of B^1_{2g} phonon mode and a high intensity of A_{1g} mode (under 633 nm excitation, compared to bulk) confirms monolayer (ref. [55])

utilized to study opto-mechanical phenomena such as inter-modal strong coupling, photo-thermal sideband cooling, and parametric self-oscillations.

Acknowledgements H.D.E acknowledges support from Army Research Office (ARO) through Grant# W911NF1510068. The authors would like to thank Dr. Chakrapani Varanasi from ARO for supporting the research program and for his inputs. L.J.L. acknowledges support of the NSF MRSEC through grants DMR-1121262 and DMR-1720139. The authors acknowledge support from the Center for Nanoscale Materials (CNM, Argonne National Lab), an Office of Science user facility, supported by the U.S. Department of Energy, Office of Science, Office of Basic Energy Sciences, under Contract No. DE-AC02-06CH11357. This work also utilized Northwestern University Micro/Nano Fabrication Facility (NUFAB), which is partially supported by Soft and Hybrid Nanotechnology Experimental (SHyNE) Resource (NSF ECCS-1542205), the Materials Research Science and Engineering Center (NSF DMR-1720139), the State of Illinois, and Northwestern University.

References

1. Wei XD, et al (2015) Plasticity and ductility in graphene oxide through a mechanochemically induced damage tolerance mechanism. Nat Commun 6:8029
2. Duerloo KAN, Ong MT, Reed EJ (2012) Intrinsic piezoelectricity in two-dimensional materials. J Phys Chem Lett 3(19):2871–2876
3. Splendiani A et al (2010) Emerging photoluminescence in monolayer MoS_2. Nano Lett 10(4):1271–1275
4. Reich ES (2014) Phosphorene excites materials scientists. Nature 506(7486):19–19
5. Mannix AJ et al (2015) Synthesis of borophenes: anisotropic, two-dimensional boron polymorphs. Science 350(6267):1513–1516
6. Lopez-Sanchez O et al (2013) Ultrasensitive photodetectors based on monolayer MoS_2. Nat Nanotechnol 8(7):497–501
7. Ye Y et al (2015) Monolayer excitonic laser. Nat Photonics 9(11): 733–737
8. Wu SF et al (2015) Monolayer semiconductor nanocavity lasers with ultralow thresholds. Nature 520(7545):69–72
9. Conley HJ et al (2013) Bandgap engineering of strained monolayer and bilayer MoS_2. Nano Lett 13(8):3626–3630
10. Desai SB et al (2014) Strain-induced indirect to direct bandgap transition in multi layer WSe_2. Nano Lett 14(8):4592–4597
11. Feng J et al (2012) Strain-engineered artificial atom as a broad-spectrum solar energy funnel. Nat Photonics 6(12):865–871
12. Zhu HY et al (2015) Observation of piezoelectricity in free-standing monolayer MoS_2. Nat Nanotechnol 10(2):151–155
13. Qi JJ et al (2015) Piezoelectric effect in chemical vapour deposition-grown atomic-monolayer triangular molybdenum disulfide piezotronics. Nat Commun 6:7430
14. Mak KF et al (2014) The valley hall effect in MoS_2 transistors. Science 344(6191):1489–1492
15. Cao T et al (2012) Valley-selective circular dichroism of monolayer molybdenum disulphide. Nat Commun. 3(887)
16. Yin XB et al (2014) Edge nonlinear optics on a MoS_2 atomic monolayer. Science 344(6183):488–490
17. Kumar N et al (2013) Second harmonic microscopy of monolayer MoS_2. Phys Rev B 87:161403
18. Wang Y et al (2017) Structural phase transition in monolayer $MoTe_2$ driven by electrostatic doping. Nature 550(7677):487–491
19. Bunch JS et al (2007) Electromechanical resonators from graphene sheets. Science 315(5811):490–493
20. Robinson JT et al (2008) Wafer-scale reduced graphene oxide films for nanomechanical devices. Nano Lett 8(10):3441–3445
21. Castellanos-Gomez A et al (2013) Single-layer MoS_2 mechanical resonators. Adv Mater 25(46):6719–6723
22. Lee J et al (2013) High frequency MoS_2 nanomechanical resonators. ACS Nano 7(7):6086–6091
23. Castellanos-Gomez A et al (2015) Mechanics of freely-suspended ultrathin layered materials. Ann Phys 527(1-2):27–44
24. Bhaskaran MKH (2015) Ultrasensitive room-temperature piezoresistive transduction in graphene-based nanoelectromechanical systems. Nano Lett 15(4):2562–2567
25. Wang ZH, Feng PXL (2015) Design of black phosphorus 2D nanomechanical resonators by exploiting the intrinsic mechanical anisotropy. 2D Materials 2:021001
26. Wang ZH et al (2016) Resolving and tuning mechanical anisotropy in black phosphorus via nanomechanical multimode resonance spectromicroscopy. Nano Lett 16(9):5394–5400
27. Mathew JP et al (2016) Dynamical strong coupling and parametric amplification of mechanical modes of graphene drums. Nat Nanotechnol 11(9):747–751
28. Liu CH, Kim IS, Lauhon LJ (2015) Optical control of mechanical mode-coupling within a MoS_2 resonator in the strong-coupling regime. Nano Lett 15(10):6727–6731
29. De Alba R et al (2016) Tunable phonon-cavity coupling in graphene membranes. Nat Nanotechnol 11(9):741–746
30. Samanta C, Gangavarapu PRY, Naik AK (2015) Nonlinear mode coupling and internal resonances in MoS2 nanoelectromechanical system. Appl Phys Lett 107:173110
31. Barton RA et al (2012) Photothermal self-oscillation and laser cooling of graphene optomechanical systems. Nano Lett 12(9): 4681–4686
32. Kumar M, Choubey B, Bhaskaran H (2017) Nanomechanical resonators show higher order nonlinearity at room temperature. arXiv: 1703.03094
33. Jiang JW, Park HS, Rabczuk T (2014) MoS_2 nanoresonators: intrinsically better than graphene? Nanoscale 6(7):3618–3625
34. Morell N et al (2016) High quality factor mechanical resonators based on WSe_2 monolayers. Nano Lett 16(8):5102–5108
35. Matis BR, Houston BH, Baldwin JW (2017) Energy dissipation pathways in few-layer MoS2 nanoelectromechanical systems. Sci Rep 7:5656
36. Li H et al (2012) From bulk to monolayer MoS_2: evolution of Raman scattering. Adv Funct Mater 22(7):1385–1390
37. Ekinci KL (2005) Electromechanical transducers at the nanoscale: actuation and sensing of motion in nanoelectromechanical systems (NEMS). Small 1(8-9):786–797
38. Novoselov KS, Castro Neto AH (2012) Two-dimensional crystals-based heterostructures: materials with tailored properties. Phys Scr T146:014006
39. Castellanos-Gomez A et al (2014) Deterministic transfer of two-dimensional materials by all-dry viscoelastic stamping. 2D Materials 1:011002
40. Blake P et al (2007) Making graphene visible. Appl Phys Lett. 91: 063124
41. Liu HL et al (2014) Optical properties of monolayer transition metal dichalcogenides probed by spectroscopic ellipsometry. Appl Phys Lett 105:201905
42. Berkdemir A et al (2013) Identification of individual and few layers of WS2 using Raman Spectroscopy. Sci Rep 3:1755
43. Carvalho BR et al (2017) Intervalley scattering by acoustic phonons in two-dimensional MoS2 revealed by double-resonance Raman spectroscopy. Nat Commun 8:14670
44. Wei XX et al (2014) Mo-O bond doping and related-defect assisted enhancement of photoluminescence in monolayer MoS_2. AIP Adv 4:123004
45. Warburton GB (1954) The vibration of rectangular plates. Proc Inst Mech Eng 168(12):371–384

46. Xiong S, Cao GX (2015) Molecular dynamics simulations of mechanical properties of monolayer MoS_2. Nanotechnology 26: 185705
47. Yoshinaka A et al (2012) Photothermal excitation of cantilevered carbon nanotube resonators. Appl Phys Express 5:075101
48. Bertolazzi S, Brivio J, Kis A (2011) Stretching and breaking of ultrathin MoS_2. ACS Nano 5(12):9703–9709
49. Garcia-Sanchez D et al (2008) Imaging mechanical vibrations in suspended graphene sheets. Nano Lett 8(5):1399–1403
50. Reserbat-Plantey A et al (2012) A local optical probe for measuring motion and stress in a nanoelectromechanical system. Nat Nanotechnol 7(3):151–155
51. Zeng H et al (2013) Optical signature of symmetry variations and spin-valley coupling in atomically thin tungsten dichalcogenides. Sci Rep 3:1608
52. Tonndorf P et al (2013) Photoluminescence emission and Raman response of monolayer MoS2, $MoSe_2$, and WSe_2. Opt Express 21(4):4908–4916
53. Zhao W et al (2013) Lattice dynamics in mono- and few-layer sheets of WS_2 and WSe_2. Nanoscale 5(20):9677–9683
54. Yamamoto M et al (2014) Strong enhancement of Raman scattering from a bulk-inactive vibrational mode in few-layer $MoTe_2$. ACS Nano 8(4):3895–3903
55. Ruppert C, Aslan OB, Heinz TF (2014) Optical properties and band gap of single- and few-layer $MoTe_2$ crystals. Nano Lett 14(11): 6231–6236